Diffuse spin waves and classical spin liquid behavior in the kagomé antiferromagnet chromium jarosite, $KCr_3(OD)_6(SO_4)_2$

Sofie Holm-Janas[1,2,3] Sidse L. Lolk,[1] Anders B. A. Andersen,[4] Tatiana Guidi,[5] David Voneshen,[5,6]
Ivica Živković,[2] Ulla Gro Nielsen,[4] and Kim Lefmann[1]

[1]*Nanoscience Center, Niels Bohr Institute, University of Copenhagen, 2100 Copenhagen, Denmark*
[2]*Laboratory for Quantum Magnetism, Institute of Physics, EPFL, 1015 Lausanne, Switzerland*
[3]*Department of Physics, Technical University of Denmark, 2800 Kongens Lyngby, Denmark*
[4]*Department of Physics, Chemistry and Pharmacy, University of Southern Denmark, 5230 Odense M, Denmark*
[5]*ISIS Facility, Rutherford Appleton Laboratory, Didcot OX11 0QX, United Kingdom*
[6]*Department of Physics, Royal Holloway University of London, Egham TW20 0EX, United Kingdom*

The dynamics of the $S = 3/2$ kagomé antiferromagnet chromium jarosite, $KCr_3(OD)_6(SO_4)_2$, was studied using high-resolution neutron time-of-flight spectroscopy on a polycrystalline sample with a nearly stoichiometric magnetic lattice [2.8(2)% Cr vacancies]. Neutron spectroscopy reveals diffuse spin wave excitations in the ordered phase with an incomplete gap and significant finite-lifetime broadening as well as a pronounced kagomé zero mode. Using linear spin wave theory, we estimate the exchange couplings. The system is highly two dimensional with the leading nearest-neighbor coupling being $J_1 = 0.881$ meV. Above T_N, diffuse excitations from the classical spin liquid regime dominate. We model the Q response and energy response separately and show that in both the ordered phase and the classical spin liquid regime they are strongly coupled.

I. INTRODUCTION

Emergent phenomena occur within geometrically frustrated spin systems, where competing interactions suppress the normal magnetic ordering of the spins and create a macroscopic ground state degeneracy with a flat energy landscape for excitations. In certain systems, this allows exotic order and disorder phenomena to emerge, such as the spin liquid [1–4]. In these states the spins fluctuate in a correlated liquid-like manner. In quantum spin liquids, the system eludes order down to temperatures of absolute zero. Furthermore, they are predicted theoretically to show long-range entanglement at 0 K [3]. However, the experimental verification of a quantum spin liquid has proven contentious, also due to inherent problems with structural defects in synthesized samples [5]. In contrast, the classical spin liquids are more prolific but studied comparatively less. Here, the frustration only partially suppresses the magnetic ordering, so that the system still orders at finite temperatures. This prevents long-range entanglement at any temperature. The interplay between order and disorder in the classical spin liquid regime, sometimes also termed the co-operative paramagnetic phase, gives rise to exotic liquid-like fluctuations at intermediate temperatures due to the frustrated interactions [4].

The kagomé antiferromagnet has taken center stage in the study of geometrically frustrated spin liquids. This is due to the two-dimensional nature and the low connectivity of $z = 4$ nearest neighbors in the kagomé geometry as illustrated in Fig. 1(b), which combined with the frustration from the antiferromagnetic couplings creates a macroscopic ground state degeneracy. The presence of dispersionless zero-energy

modes in the ground state manifold prevents long-range order even at $T = 0$, both in the classical and quantum spin system [6]. These zero-energy modes (dubbed *kagomé zero modes*) are a special property of the kagomé geometry and originate from the fact that coherent local rotations of the spins in two sublattices around the third may occur at no energy cost [6]. In most physical realizations of the kagomé antiferromagnet the presence of additional, nondominant interactions will cause the systems to order magnetically at finite temperatures. These additional interactions will cause the zero-energy mode to be lifted up to finite energy transfers, which has the fortunate consequence that they can be observed more easily in neutron experiments. In spite of this, the kagomé zero mode has only been observed so far in three classical kagomé antiferromagnets [7–9].

One of the most studied classical kagomé antiferromagnetic materials is the jarosite family of magnets with the general chemical composition $AM_3(OH)_6(SO_4)_2$, where A is a monovalent ion (Na^+, K^+, H_3O^+, Ag^+, or NH_4^+) and M is a trivalent ion, which may be magnetic (Fe^{3+}, Cr^{3+}, or V^{3+}). Jarosites crystallize in the $R\bar{3}m$ space group with magnetic ions positioned in stacked kagomé planes, as shown in Fig. 1. Jarosite originally refers to the $S = 5/2$ iron mineral $KFe_3(SO_4)_2(OH)_6$ (henceforth referred to as Fe-jarosite), which is a frustrated antiferromagnet and orders at $T_N = 65$ K. Fe-jarosite is well described as a Heisenberg antiferromagnet with a Dzyaloshinskii-Moriya (DM) interaction, which causes a spin canting within the kagomé layers [10]. The magnetic properties of Fe-jarosite have been studied extensively [7,10–16], both as powders and as single-crystal specimens. Changing the magnetic ion to V^{3+} lifts the frustration and
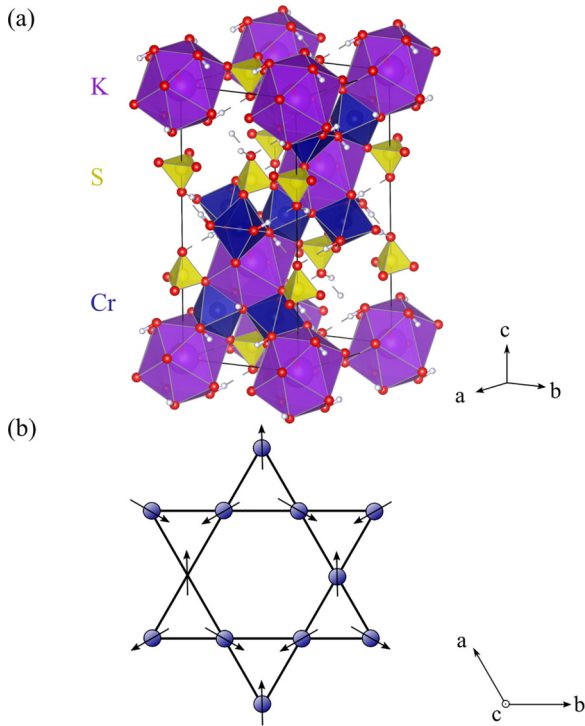
(a)

(b)

FIG. 1. (a) Crystal structure of Cr-jarosite. (b) Magnetic ground state in the 120° configuration in the two-dimensional chromium kagomé planes.

causes ferromagnetic ordering in V-jarosite [17,18]. However, markedly fewer studies have addressed the magnetic behavior of the $S = 3/2$ Cr analog, $KCr_3(OH)_6(SO_4)_2$ (Cr-jarosite). Cr-jarosite is also a frustrated antiferromagnet [19–21] and is the focus of this paper.

Studies of jarosites, and in particular of Cr-jarosite, have suffered significantly from the difficulty in synthesizing pure and stoichiometric compounds. This is a general and significant problem for many frustrated materials, in which structural disorder and defects complicate the analysis of the weak magnetic behavior [5]. However, this was improved for jarosites by the introduction of the redox-hydrothermal synthesis in the early 2000s [10,11,17] for $M = $ Fe and V. For jarosites, the two main defects are a vacancy on the magnetic B site and mixed occupancy on the A site, which may or may not be correlated [19,22]. An M site vacancy will locally destroy the kagomé lattice by lifting the magnetic frustration, leading to local antiferromagnetic interactions and an A site vacancy [23]. It is an experimental fact that while Fe-jarosites with $A = K^+$, NH_4^+, Na^+, or Ag^+ will order magnetically, jarosites with $A = H_3O^+$ instead show spin glass behavior. Thus the A site cations also affect the magnetic properties, but currently an understanding of the mechanism is lacking [24–28]. Although the redox-hydrothermal synthesis has improved the stoichiometry, our recent study of Cr-jarosite prepared using this approach revealed significant (2–27%) substitution of K by D_3O^+ and D_2O species [19].

While the static magnetic behavior of Cr-jarosite has previously been contested (see, e.g., Refs. [29–32]), all recent results [19–21] point to the same overall conclusions: Cr-jarosite orders antiferromagnetically at $T_N \approx 4$ K and has a

Curie-Weiss temperature of $\theta_{CW} \approx -62$ K, resulting in a frustration ratio of $f = |\theta_{CW}|/T_N \approx 16$ [19]. Below T_N it assumes a 120° noncollinear ground state with a small ferromagnetic canting in each layer due to a small DM interaction; see Fig. 1(b) [19–21]. The kagomé layers are coupled ferromagnetically, causing the spins to cant the same way in each layer, which adds up to a small positive magnetization. However, the excitations in Cr-jarosite have only previously been investigated in a single study made before the advent of the redox-hydrothermal synthesis on a sample with 26% Cr vacancies and an undisclosed amount of K vacancies [33]. Such a high Cr vacancy content significantly affects the magnetism of the sample, as 33% Cr vacancies completely lift the magnetic frustration, making this previous study not representative of stoichiometric Cr-jarosite.

In this paper we will study the classical spin liquid compound Cr-jarosite and remedy the lack of excitation studies by use of neutron spectroscopy on a well-defined sample with a stoichiometric magnetic lattice. The vacancy levels were quantified using ^{2}H magic angle spinning nuclear magnetic resonance (MAS NMR), which is highly sensitive to local environments within the crystal lattice and therefore ideal as a tool for defect quantification. In the ordered state below T_N, the excitation spectrum can be described by dampened spin waves which are modeled using linear spin wave theory to extract estimates of the exchange interactions. In the classical spin liquid regime above T_N the excitations are of a short-ranged nature. By modeling both the energy dependence and the Q dependence of the excitations we link the behavior to that of a classical spin liquid.

II. EXPERIMENTAL DETAILS

Polycrystalline, deuterated Cr-jarosite, $KCr_3(OD)_6(SO_4)_2$, was prepared by the redox-hydrothermal method [10] with a combined mass of 6.9 g. The purity of the sample as well as each batch prior to mixing was assessed by powder x-ray diffraction (PXRD) and ^{2}H MAS NMR. The synthesis and characterization followed our recently reported procedure [19], with further details given in Appendix A.

^{2}H MAS NMR single-pulse and rotor-synchronized Hahn-echo (90°–τ–180°–τ–acquisition) spectra were performed on an Agilent INOVA spectrometer at 14.1 T equipped with a 1.6-mm triple-resonance MAS probe using several spinning speeds in the range 30–35 kHz for unambiguous identification of the isotropic regions; see Ref. [19]. The echo delay τ was one rotor period. The ^{2}H MAS NMR spectra were referenced relative to tetramethylsilane (TMS) using D_2O ($\delta_{iso} = 4.6$ ppm) as a secondary reference. The ^{2}H MAS NMR data were processed using MestReNova software (version 12.0.1). Spectral deconvolution and fitting of the chemical shift anisotropy (CSA) parameters (Δ and η_σ) and quadrupole coupling (C_Q and η_Q), were performed using ssNake software [34] (version 1.2); see Ref. [19]. The CSA parameters are reported in the Haeberlen convention [35], where the Euler angle β relates the principal axis of the CSA and quadrupole tensor [36].

Susceptibility data were measured between 5 and 370 K using a Quantum Design Magnetic Property Measurement System 5 (MPMS-5) superconducting quantum interference

device (SQUID). Low-temperature measurements of the magnetization were performed using a Quantum DynaCool Physical Property Measurement System (PPMS).

Neutron spectroscopy was performed at the ISIS neutron facility (Didcot, United Kingdom). Initially, the excitations were studied using the time-of-flight spectrometer MARI using a He-4 cryostat [37], which revealed a need for better low-energy resolution. Thus we proceeded to the time-of-flight spectrometer LET (ISIS) [38], where the powder was loaded into a hollow cylindrical aluminum canister in a helium atmosphere and placed in an orange-type cryostat. Repetition rate multiplication energies of 2.20, 3.70, 7.60, and 22.20 meV provided simultaneous access to different parts of the reciprocal space. For investigations of Bragg reflections, $E_i = 2.20$ meV was used for slightly better Q resolution, while $E_i = 3.70$ meV data are used for all other investigations as the best compromise between resolution and (Q, ω) coverage of the excitations. Data were taken at nine different temperatures between 1.8 and 100 K. The initial data reduction was performed with MANTID [39], and data analysis was performed using HORACE [40]. Data modeling of spin waves was performed using a linear spin wave theory based on the Holstein-Primakoff framework as implemented in the SPINW package [41].

III. CHARACTERIZATION

PXRD and scanning electron microscopy with energy dispersive spectroscopy (SEM-EDS) were used to determine the purity and chemical composition of the combined sample. The PXRD diffractograms (see Appendix B) showed only reflections from chromium jarosite and are in excellent agreement with our recent study [19]. Thus no crystalline impurities were identified by PXRD. It is noted that the (107) reflection shows a complex line shape indicative of partial hydronium substitution on the K site, as discussed in detail in Ref. [19].

The concentration of defects was quantified by ^{2}H MAS NMR spectroscopy for the combined sample following the same procedure as earlier reported [19]. The Cr and K defects have previously been shown to be correlated and can be summarized in the general chemical formula as [19]

$$[K_{1-x-y}(D_nO)_{y+x}]Cr_{3-x}(SO_4)_2(OD)_{6-4x}(OD_2)_{4x}, \quad (1)$$

where D_nO refers to the total concentration of deuterium species on the A site, which is the sum of D_2O and D_3O^+. This highlights that Cr vacancies also cause K vacancies, but K vacancies can also occur on their own by substitution of K^+ with D_3O^+. The concentration of the defects may be determined by deconvolution of the ^{2}H MAS NMR spectrum (see Appendix D). The Cr vacancies are then determined from the integrated intensities of the appropriate ^{2}H NMR resonances [22]:

$$4x = 6\frac{\frac{1}{2}I(CrOD_2)}{I(Cr_2\text{-}OD) + \frac{1}{2}I(CrOD_2)}. \quad (2)$$

The average number, n, of deuterons on the A site may similarly be estimated by [22]

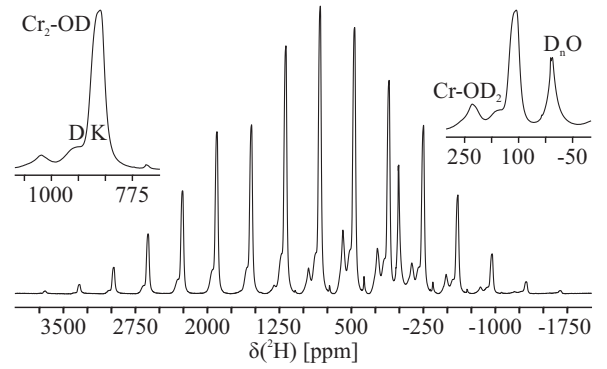$$n = 6\frac{I(D_nO)}{I(Cr_2\text{-}OD) + \frac{1}{2}I(Cr\text{-}OD_2)}, \quad (3)$$

FIG. 2. ^{2}H MAS NMR spectrum (Hahn echo) of polycrystalline Cr-jarosite recorded at 14.1 T with 33 kHz spinning speed. The left inset illustrates the isotropic region for the Cr_2-OD (D) and Cr_2-OD (K) resonances. The right inset shows the isotropic region for the Cr-OD_2 and D_nO resonances.

where values of $n = 3$, 2, or 0 correspond to the A site being fully occupied by D_3O^+, D_2O, or K^+, respectively.

The ^{2}H MAS NMR spectrum (Fig. 2) contains the spinning-sideband manifold for four resonances located at $\delta_{iso} = 872(10)$, 828(5), 229(5), and 7(2) ppm, which are assigned to Cr_2-OD (D), Cr_2-OD (K), Cr-OD_2, and D_nO, respectively, using earlier reported data [19,42]. The Cr_2-OD resonances stem from stoichiometric Cr-jarosite with either D_nO or K^+ on the A site. The Cr-OD_2 resonance stems from there being a Cr next to a Cr vacancy (defect), whereas the D_nO resonances contain the overlapping resonances from D_nO on the A site and surface adsorbed D_2O. Moreover, a negligible amount ($<1\%$) of a sharp D_nO resonance at 11(1) ppm from an unknown impurity was observed. Thus the ^{2}H MAS NMR spectra also confirm partial substitution of hydronium in the sample.

Based on these values, Eq. (2) yields $x = 0.085(1)$, corresponding to 2.8(2)% Cr vacancies [97.2(2)% occupancy on the magnetic lattice]. Equation (3) yields $n = 0.41(9)$ and thereby a K occupancy of 80–86%, where the upper and lower boundaries correspond to substitution by only D_3O^+ or D_2O on the A site, respectively. Thus the analysis of the combined sample by PXRD, SEM-EDS, and ^{2}H MAS NMR confirms the formation of Cr-jarosite. Based on the quantified level of defects, the magnetic kagomé lattice of Cr ions is almost perfectly intact. The K defects are at a quantified level and match our earlier study [19].

The susceptibility was measured from 5 to 370 K in applied fields of 3 T; see Fig. 3(a). Fitting the data with the Curie-Weiss law and assuming $g = 1.97$ as determined from electron spin resonance (ESR) [21] yields a Curie-Weiss temperature of $\theta_{CW} \approx -58$ K, in close agreement to previously obtained values [19,20]. Assuming that the nearest-neighbor interactions within the kagomé plane dominate, a mean-field estimate for the in-plane exchange coupling can be obtained as

$$J_{MF} = \frac{3k_B|\theta_{CW}|}{zS(S+1)} \approx 1.0 \text{ meV}, \quad (4)$$

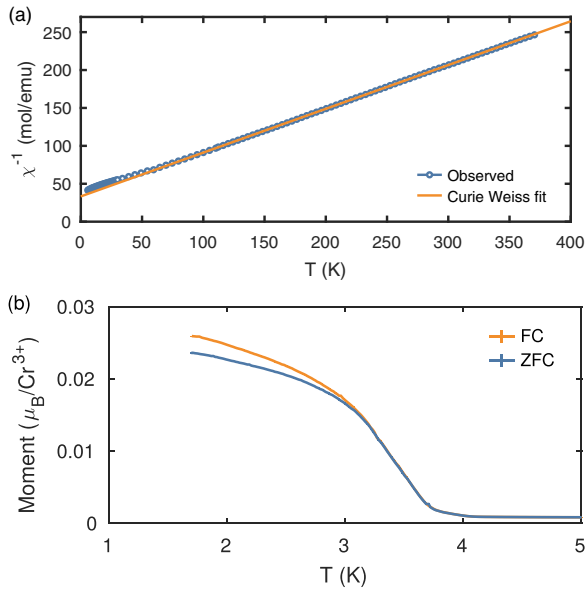where $z = 4$ is the number of nearest neighbors.

FIG. 3. Magnetization of Cr-jarosite. (a) Inverse molar susceptibility measured in 3 T fitted with the Curie-Weiss law. (b) Magnetization in 0.02 T field.

The field-cooled (FC) and zero-field-cooled (ZFC) magnetizations of the sample for low temperatures in 0.02 T are shown in Fig. 3(b), which shows an antiferromagnetic phase transition with weak ferromagnetic canting in the region 3–4 K. The FC and ZFC magnetizations show a small difference at low temperatures, consistent with the hysteresis in the system due to the canted antiferromagnetic moment [19]. At 1.7 K, the magnetization is measured as 0.024 μ_B/Cr^{3+} in the powdered sample, corresponding to 0.05 μ_B/Cr^{3+} in a single crystal with magnetic field along the c axis, matching previous results [19,20]. Assuming a saturated magnetization of 3.87 μ_B for Cr^{3+} in an octahedral ligand field, this corresponds to a spin canting angle of approximately $\alpha = \sin^{-1}(M/M_s) \approx 0.7°$. The magnetic and structural Bragg reflections in Cr-jarosite were investigated to ascertain the magnetic ordering (Fig. 4). These elastic scattering data were obtained from the LET data with $E_i = 2.20$ meV by taking constant-energy cuts around the elastic line. Figure 4(a) shows the intensity difference between 1.8 K and 4 K and highlights the purely magnetic Bragg reflections. All reflections can be indexed by hand using a magnetic unit cell identical to the structural unit cell. This is consistent with a ground state with the 120°, **q** = 0 spin arrangement with a small ferromagnetic canting out of the kagomé plane. Note that no actual Rietveld refinement of the structure is possible due to the poor resolution and Q coverage of spectrometer data compared with actual diffractometer data. Figure 4(b) shows the low-temperature evolution of the intensity of the magnetic (012) reflection. This is consistent with both the susceptibility measurements in Fig. 3 and the results of $T_N = 3.8$ K from our previous neutron investigation [19] for samples with a similar vacancy profile.

IV. MAGNETIC EXCITATIONS

The excitation spectra for the lowest measured temperature can be seen in Fig. 5 for data using $E_i = 7.60$ meV, showing
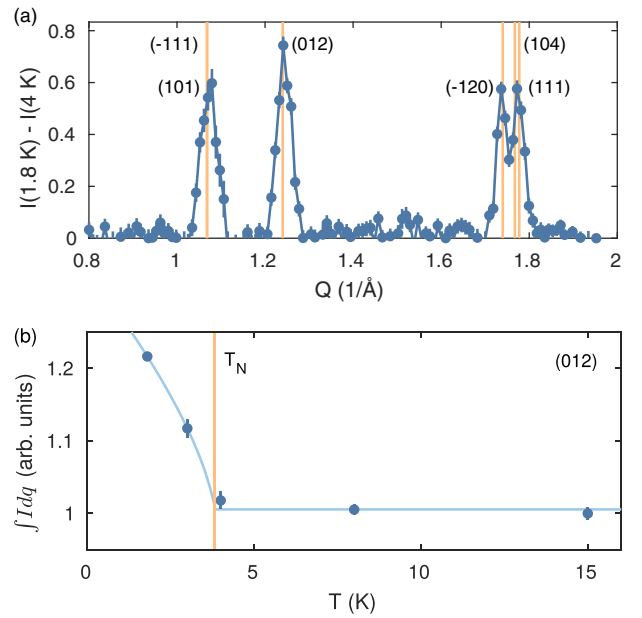

FIG. 4. Elastic scattering from Cr-jarosite measured on LET. Data are obtained using $E_i = 2.20$ meV and integrated in the energy transfer range $\Delta E = \pm 0.08$ meV. (a) Difference between the elastic line at 4 K and the elastic line at 1.5 K with indexed magnetic Bragg peaks. (b) Temperature vs integrated intensity for the purely magnetic (012) reflection around $Q = 1.25$ 1/Å. The blue line is a guide-to-the-eye power law fit with $T_N = 3.8$ K.

that all relevant magnetic excitations appear at energies below 4 meV. Thus the analysis of the excitations will focus on the lower energies accessed with $E_i = 3.70$ meV.

The temperature development of the excitation spectra can be seen in Fig. 6. In the magnetically ordered phase at $T = 1.8$ K $\approx T_N/2$ [Fig. 6(a)], distinct spin wave excitations can be seen. The data reveal a continuum of high intensity scattering centered at $Q \approx 1.1$ Å^{-1} and $\hbar\omega = 0.7$ meV with indications of a gap. The spin wave branches continue up to roughly 4 meV as seen in Fig. 5. Additionally, a gapped, broad, and approximately flat mode exists at $\hbar\omega = 0.4$–0.9 meV extending up to $Q \approx 3.5$ Å^{-1}. As shall be shown later, this flat mode
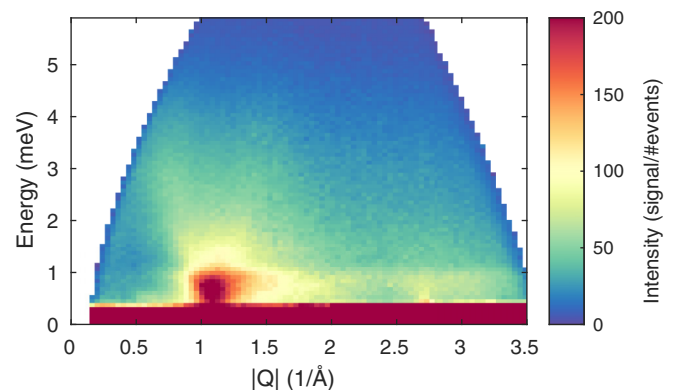

FIG. 5. Excitations at 1.8 K in Cr-jarosite measured using neutron spectroscopy at LET with $E_i = 7.60$ meV.
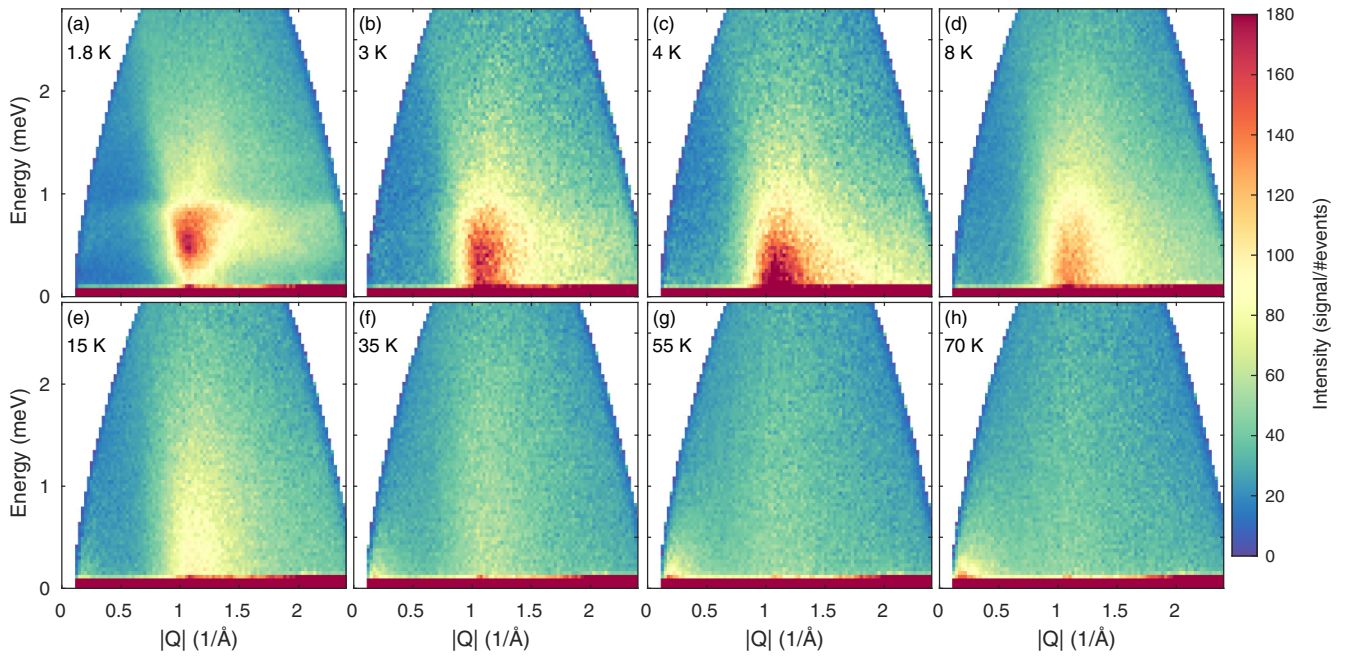
FIG. 6. (a)–(h) Excitation spectra in Cr-jarosite measured by inelastic neutron scattering at LET for various temperatures using $E_i = 3.70$ meV.

is a realization of a kagomé zero mode lifted to finite energies due to the DM interaction.

Beginning from the low-temperature data, the intensity moves towards lower energies as the temperature increases from 1.8 K through T_N, and the spectra start to lose the distinct spin waves. Above T_N, the excitations remain as a distinct feature with intensity above $Q \approx 1.1$ Å^{-1} and no gap to the elastic line visible in the $E_i = 3.70$ meV data. This feature remains visible up to $\sim$15–35 K. Some broader, increased intensity is also present at 55–70 K, which can be recognized as paramagnetic scattering that is practically constant within the energy scale of the system and decreases in a way consistent with the magnetic form factor for larger Q. From 35 to 70 K, increased low-energy intensity for very low Q appears. Due to its temperature dependence, we believe this to be related to structural small-angle scattering and have not included this further in the analysis.

The distinct excitations in the range $\sim$4–15 K are magnetic in nature, as they are continuously connected to the spin wave excitations at low temperatures, disappear at higher temperatures, and originate from the position of the strong magnetic Bragg reflections. Given their diffuse nature, they indicate short-ranged magnetic correlations within the classical spin liquid regime.

The existence of a gap in the excitation spectrum is illustrated in Fig. 7, where Fig. 7(a) shows a cut through the strong continuum centered at $Q \approx 1.1$ Å^{-1}, while Fig. 7(b) shows a cut through the lifted kagomé zero mode at higher Q. For the spin wave continuum above the (101) reflection, the gap appears incomplete even at 1.8 K, although it may open fully at lower temperatures. The gap is still vaguely present in the 3 K data, while being completely closed at 4 K. The gap from the elastic line to the kagomé zero mode around $Q \approx 2$ Å^{-1} [Fig. 7(b)] is, however, a complete gap with a

value of $\sim$0.4 meV at 1.8 K. As the temperature increases, this gap also closes.

A. Spin waves

Figure 8(a) shows the measured spin wave spectrum well within the ordered phase at $T = 1.8$ K. We will analyze the
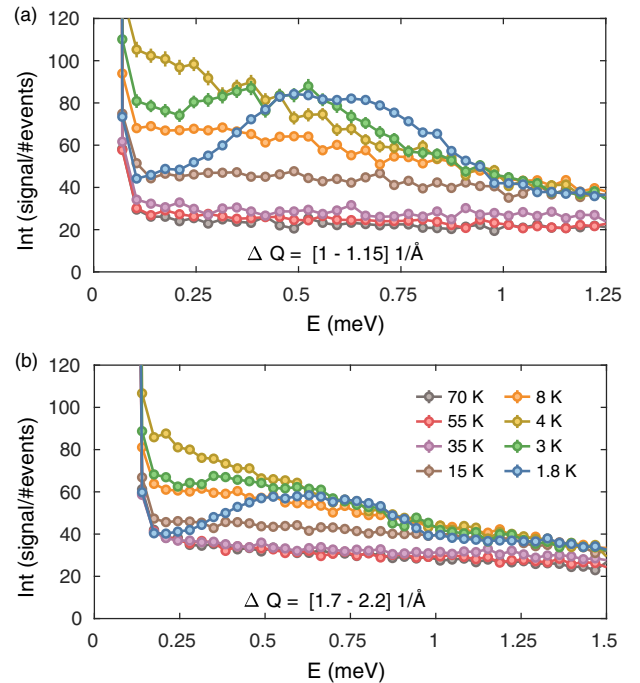

FIG. 7. Constant-Q cuts through the excitations integrated over energy for various temperatures. (a) Cut through the intense excitation at $Q \approx 1.07$ Å^{-1} with $E_i = 2.20$ meV. (b) Cut through the flat mode at $Q \approx 2$ Å^{-1} with $E_i = 3.70$ meV.
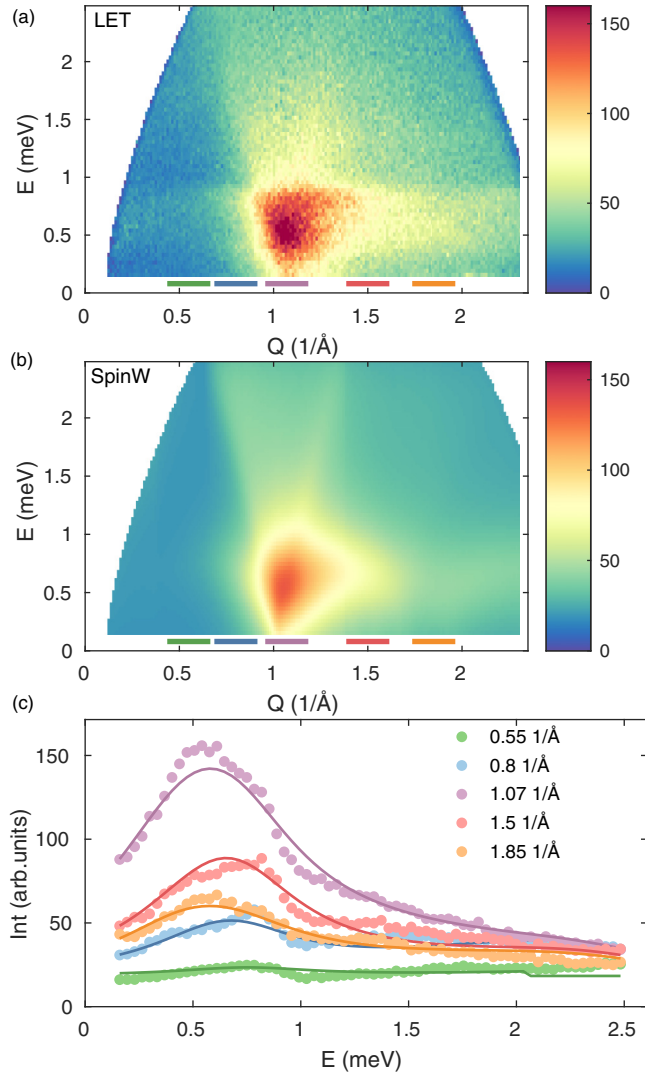
FIG. 8. Spin wave excitations in Cr-jarosite. (a) Spin waves measured with LET at $T = 1.5$ K. (b) Resulting SPINW spectra of best fit. (c) Simultaneous SPINW fit of Q cuts through data as described in the text. The positions and widths of the Q cuts are indicated in (a) and (b) with horizontal colored lines.

excitations in the ordered state with linear spin wave theory to obtain estimates for the exchange couplings. The spin wave excitations in Fig. 8(a) lack any clear Van Hove singularities and appear to be significantly broadened. This may either stem from finite lifetimes of the spin waves, which would cause a broadening in energy, or stem from coexisting, persistent short-ranged correlations, which would cause a broadening in Q. Both of these effects are inherent to frustrated lattices but may also be exacerbated by the K disorder in the sample, which may also cause diffuse scattering. No matter the precise origin, the effects on the data will be similar. For technical reasons, related to calculating powder averages using SPINW, we will assume an energy broadening of the spin waves as stemming from finite lifetimes.

We assume the magnetic ground state to be the $120°$, $\mathbf{q} = 0$ spin structure with equal canting in each layer. We assume the

magnetic system to be described by the Hamiltonian

$$\mathcal{H} = \sum_{\mathrm{nn}} [J_1 \vec{S}_i \cdot \vec{S}_j + \vec{D}_{ij} \cdot \vec{S}_i \times \vec{S}_j]$$
$$+ \sum_{\mathrm{nnn}} J_2 \vec{S}_k \cdot \vec{S}_l + \sum_{\mathrm{n}_\perp \mathrm{n}_\perp} J_\perp \vec{S}_m \cdot \vec{S}_n, \quad (5)$$

where J_1 and J_2 are the in-plane nearest- and next-nearest-neighbor antiferromagnetic exchange couplings, while $J_\perp$ is the interlayer nearest-neighbor coupling. $J_\perp$ is constrained to be ferromagnetic due to the ordered state having the same in-plane spin arrangement in neighboring layers. $\vec{D}_{ij} = [\sqrt{3} D_y(i, j), D_y(i, j), D_z(i, j)]$ is the symmetry-allowed DM interaction, where we also assume both $D_y < 0$ and $D_z < 0$. While the exact role of the exchange parameters was found analytically by Yildirim and Harris [43], their overall contribution can be summarized as follows: J_1 controls the bandwidth of the high-intensity, higher-energy spin wave, D_y and D_z control the center of the flat mode and cause a canting of the spins, and J_2 causes dispersions of the flat mode, such that D_y, D_z, and J_2 together control the bandwidth of this mode. $J_\perp$ is not included in the analytical treatment, but small $J_\perp$ also induces dispersions in the flat mode.

The spin wave dispersions were calculated using the SPINW package and then powder-averaged to compare with experimental data. In order to account for the experimental resolution along Q, the powder-averaged spectra were convoluted with a Gaussian with full width at half maximum (FWHM) of $\Delta Q = 0.1$ Å^{-1} as estimated from the width of the Bragg reflections. In order to account for the overall smearing modeled by the finite lifetimes of the excitations, an additional variable parameter is introduced by convolution of the spectra with a Lorentzian with FWHM ΔE. We used a constrained particle swarm algorithm to perform χ^2 fitting of constant-Q cuts through the data. To capture most features of the spin waves while also keeping run times manageable, we simultaneously fitted five cuts through Q at $Q = 0.55$, 0.8, 1.07, 1.5, and 1.85 Å^{-1} with width $dQ = 0.1$ Å^{-1}, as illustrated in Fig. 8. We fitted the data using seven free parameters: J_1, J_2, $J_\perp$, D_y, and ΔE, as well as a common intensity scale and constant background. We assumed that the DM interaction had the same $D_z/D_y = 0.255$ ratio as the values obtained by Okubo *et al.* [21] based on antiferromagnetic resonance measurements, but we allowed the strength to vary. The next-nearest-neighbor J_2 was included in the fit since it significantly improved the reduced χ^2 of the fit. The spin canting was optimized for each choice of the exchange parameters to minimize the ground state energy.

The resulting best fit can be seen in Fig. 8. Figure 8(a) shows the experimental spectrum, Fig. 8(b) shows the resulting SPINW spectrum, and Fig. 8(c) shows the five one-dimensional (1D) cuts that the fit was made to. The best fit has the parameters $J_1 = 0.881$ meV, $J_2 = 0.015$ meV, $J_\perp = -0.0003$ meV, $D_y = -0.025$ meV, and $D_z = -0.006$ meV and a Lorentzian broadening of $\Delta E = 0.73$ meV for a combined reduced χ^2 of 17.1. We note that there is no attempt to quantify any errors on the best-fit parameters, since systematically mapping out the six-dimensional χ^2 landscape related to the fit is beyond the scope of this paper.

The fit captures the dominant features of the spin waves quite well, as is especially evident in Fig. 8(c) of the actual fit. The fit highlights that the system is highly two dimensional, since $J_\perp$ is not significantly different from zero. We note that J_2 is required to satisfactorily model the spin waves. A key feature of the fit is the Lorentzian broadening in energy, $\Delta E = 0.730$ meV. This is 20 times larger than the instrumental resolution of the elastic line, $\delta E = 0.082$ meV, and will be discussed in detail in Sec. V B. When the ground state is optimized, SPINW achieves a 120° spin structure as expected with a spin canting angle of 1.06° out of the kagomé plane. This matches well with the canting angle estimated from our magnetization measurements of 0.7°. Furthermore, the sum of all exchange interactions from SPINW matches well with the mean-field $J_{MF} \approx 1.0$ meV estimate from the susceptibility data.

B. Diffuse excitations above T_N

For $T > T_N$ the diffuse excitations in the range 0–3 meV persist, and above ~ 35 K ($> 9\,T_N$) the signal resembles a simple, paramagnetic background. We will attempt to model the excitations above T_N by describing the excitations along the energy and Q axes, separately.

1. Energy dependence

The temperature evolution of constant-Q cuts around the magnetic Bragg reflection at 1.1 Å^{-1} is shown in Fig. 9. The data can be modeled assuming a quasielastic behavior with broadening in energy due to finite lifetimes and a damped harmonic oscillator (DHO) to account for the inelastic response at low temperatures [8,44]. Thus we fit the data with the following model:

$$S(\omega, T) = S_E(\omega, T) + S_{QE}(\omega, T) + S_{DHO}(\omega, T), \quad (6)$$

where $S_E(\omega, T)$ is a Gaussian to account for the elastic line. $S_{QE}(\omega, T)$ is the quasielastic response as modeled by an exponential spin relaxation in the form of a Lorentzian

$$S_{QE}(\omega, T) = \frac{1}{1 - e^{-\hbar\omega/k_B T}} \frac{\chi_0 \omega \Gamma}{\omega^2 + \Gamma^2}, \quad (7)$$

where the first term represents the detailed balance factor describing the thermal population of excited states, Γ is the energy linewidth, and χ_0 is the static susceptibility. The inelastic response $S_{DHO}(\omega, T)$ is fitted by a damped harmonic oscillator (DHO) including detailed balance factor and corresponding to the double Lorentzian

$$S_{DHO}(\omega, T) = \frac{1}{1 - e^{-\hbar\omega/k_B T}} \frac{A_{DHO}\omega\Gamma}{\left(\omega^2 - \omega_{DHO}^2\right)^2 + (\omega\Gamma)^2}, \quad (8)$$

where A_{DHO} is the oscillator strength and ω_{DHO} is the eigenfrequency. $S_{DHO}(\omega, T)$ is only included in the fit for 4 K and below, since the scattering above could easily be reproduced without the inelastic response.

The fit to data is shown in Fig. 9 and shows that the inelastic response at low temperatures is pronounced but decreases steadily as the temperature increases. Simultaneously, the energy linewidth Γ, which is common to both $S_{QE}(\omega, T)$ and $S_{DHO}(\omega, T)$, increases as the temperature increases as expected. It should be noted that the linewidth at 1.8 K of
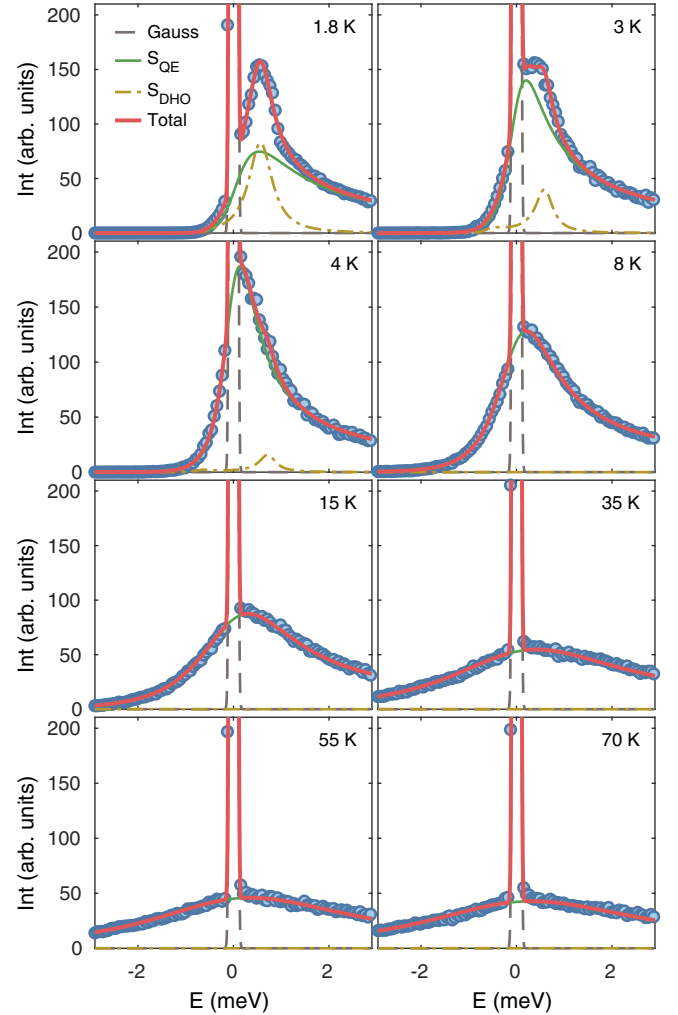

FIG. 9. Constant-Q cuts at 1.1 ± 0.1 Å^{-1} fitted with the damped harmonic oscillator model of Eq. (6).

$\Gamma = 0.6 \pm 0.2$ meV is consistent with the energy broadening obtained by the SPINW model of 0.73 meV.

2. Q dependence

The temperature evolution of the Q dependence of the excitations may reveal information about the short-ranged nature of the correlations. Figure 6 shows the Q dependence of the excitations for various temperatures obtained by integrating the spectroscopy data for excitations above the elastic line. The data show a very broad and asymmetrical peak at $Q \approx 1.1$ Å^{-1}. The diffuse appearance and the broadness in Q of the excitations indicate short-ranged magnetic correlations. These excitations are strongest for the lowest temperatures but persist until around 35 K $\approx |\theta_{CW}|/2$, much above T_N. Due to the dominating in-plane couplings between spins, we hypothesize that this behavior arises from short-ranged correlations that are purely two dimensional and occur between spins within the kagomé planes. In order to model this, we employ a heuristic model for obtaining powder averages of 2D excitations with characteristic length scale ξ.

In this model, we assume that the 2D excitations will occur around the 2D ordering vector $(hk) = (10)$ located at $Q_0 = 1.005$ Å^{-1}, but with constant intensity independent of the l component of **Q**. This 2D scattering rod must then be powder-averaged in three-dimensional (hkl) space. The geometrical derivation of this can be found in Appendix E and yields an effective expression for the powder-averaged Q dependence of the intensity as $I(Q) \propto 1/(Q\sqrt{Q^2 - Q_0^2})$ for $Q > Q_0$ and zero for $Q < Q_0$. The divergence at $Q = Q_0$ is essentially of a square root type and thus integrable. Our result is identical to the treatment of Yang and Frindt [45], which is an improvement of the classical Warren function [46], valid for powder-averaged diffraction of a 2D system. To account for the short-ranged correlations of our magnetic system, we perform a convolution of the expression with a Lorentzian with a full width at half maximum given by $\gamma = 1/\xi$, where ξ is the correlation length. Thus the resulting convoluted line shape is

$$S(Q, T) = C_L(Q, T) = |f(Q)|^2$$
$$\times \int_0^\infty \frac{1}{Q'\sqrt{Q'^2 - Q_0^2}} \frac{\gamma^2}{(\gamma/2)^2 + (Q' - Q)^2} dQ',$$
$$(9)$$

where $f(Q)$ is the magnetic form factor for Cr^{3+}. The equation is fitted to the data including an overall scaling parameter and a variable background. In our data analysis, γ is sufficiently broad that convolution with an experimental resolution function is unnecessary.

The fitting of this model to the data can be seen in Fig. 10, which shows the Q dependence of the data integrated from 0.11 to 2.5 meV, i.e., the excitations above the elastic line. Temperatures above 55 K $\approx |\theta_{CW}|$ have not been fitted due to a lack of distinct features. For the lower temperatures, our simple model works remarkably well, as it reproduces both the peak position and the asymmetric line shape: both in the classical spin liquid regime and below T_N. The temperature dependence of the effective 2D correlation length ξ is shown in Fig. 10(b). At the highest fitted temperature, 55 K, we find $\xi \approx 4$ Å, which is close to the distance between nearest-neighboring Cr atoms in the kagomé plane of 3.65 Å. The correlation length increases for decreasing temperature and reaches $\xi \approx 17$ Å at 1.8 K, which corresponds to 4.6 times the separation distance of the Cr atoms.

V. DISCUSSION

A. Effects of the sample quality

Our sample has 2.8% magnetic Cr^{3+} vacancies. This is significantly closer to stoichiometry than the only other sample measured with neutron spectroscopy, which had 26% vacancies [33]. Furthermore, our sample has 14–20% K$^+$ vacancies that may be replaced by either D$_2$O or D$_3$O$^+$. Lee *et al.* [33] did not quantify this value, but it is unlikely that their K vacancies are significantly smaller than ours. Thus this study is the best current measurement of excitations in Cr-jarosite.

For the iron-analog jarosites, it is well established that (H$_3$O)Fe$_3$(SO$_4$)$_2$(OH)$_6$ is a spin glass [24,25,28], and fur-
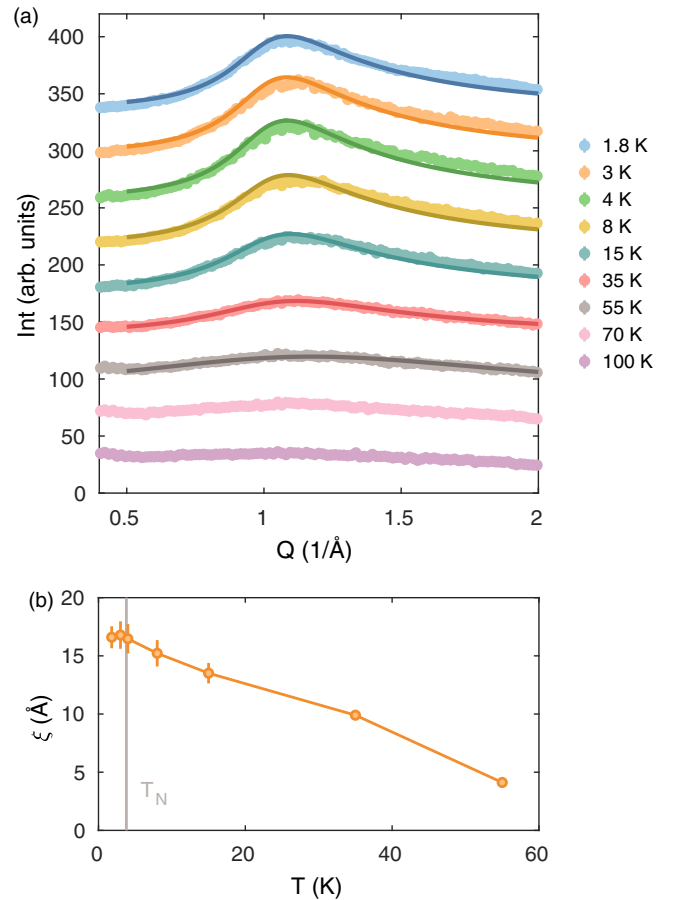

FIG. 10. (a) Q dependence of data integrated in the range 0.11–2.5 meV for various temperatures. Solid lines are fits to Eq. (9). Each temperature has been offset for clarity. (b) Resulting correlation length.

thermore, the magnetic behavior changes gradually between the 120° antiferromagnetic (AFM) order in KFe$_3$(SO$_4$)$_2$(OH)$_6$ and the spin glass behavior of (H$_3$O)Fe$_3$(SO$_4$)$_2$(OH)$_6$ with increasing H$_3$O$^+$ content [25]. For the Cr analogs, the precise magnetic behavior of (H$_3$O)Cr$_3$(SO$_4$)$_2$(OH)$_6$ remains largely unexplored, although it also shows hints of spin glass behavior [6,31,32]. Assuming that hydronium defects act in a similar manner in both Cr and Fe analogs, the level of K vacancies in our sample will certainly have some effect on the magnetic ordering. Assuming that the vacancies are approximately randomly located throughout the lattice, this could lead to a distribution of exchange interactions. The consequence of this will likely be increased levels of diffuse scattering, which is hard to distinguish from what is caused by the frustration in the kagomé lattice.

B. Spin waves and coupling constants

The resulting exchange parameters as obtained from powder-averaged linear spin wave theory are summarized in Table I, where they are compared with values from the literature. Our exchange parameters improve on the previously published estimates of the exchange couplings, as our model includes all the interactions simultaneously. The value of

TABLE I. Exchange couplings, energy broadening, and spin canting for Cr-jarosite estimated in the literature and from the SPINW simulation of our data based on the Hamiltonian in Eq. (5). All values are given in units of meV, unless otherwise stated.

	Method	J_1	J_2	$J_\perp$	D_y	D_z	ΔE	Canting (deg)
Lee *et al.* [33]	Susceptibility	1.21						
Okuta *et al.* [20]	Susceptibility	1.06						0.86
Okubo *et al.* [21]	Antiferromagnetic resonances				−0.0470	−0.0120		1.44
This paper	Neutron spectroscopy	0.881	0.015	−0.0003	−0.025	−0.006	0.73	1.06

the nearest-neighbor coupling parameter, J_1, is around 17% smaller than previously estimated by magnetization measurements [20]. However, our inelastic neutron spectroscopy is expected to be a much more precise estimator. The DM coupling we obtain via SPINW is almost 50% lower than that determined by electron spin resonance (ESR) [21]. However, we expect ESR to provide an order-of-magnitude estimate, and in this regard it matches our DM interactions well. The spin wave spectrum calculated with the same parameters but using the DM couplings suggested by Ref. [21] decreases the match with data significantly. Furthermore, our results indicate that $J_\perp$ does not differ significantly from zero within the uncertainty of the fit. Furthermore, the spin canting angle of 1.06° obtained by the SPINW model agrees with both our estimate from the susceptibility data of 0.7° and the canting angles measured in the literature in the range 0.86°–1.44° [20,21].

The spin waves appear diffuse in both Q and $\hbar\omega$. A number of possible, nonexclusive reasons for this exist: It could indicate a broadening due to finite lifetimes of the excitations, caused by the frustration in the lattice or by the relatively low spin value ($S = 3/2$); or it could indicate a distribution of exchange interactions due to randomly located vacancies at the A site. Our SPINW model takes this into account in an effective way by including the Lorentzian broadening, ΔE.

The intense spin wave feature at $Q \approx 1.1$ Å^{-1} has an incomplete gap, but the flat mode has a full gap of ~0.2 meV. Both gaps close at $T_N \approx 3.8$ K. Our measurement thus provides evidence of the flat kagomé zero mode lifted to finite energies by the DM interaction, so far only observed in iron jarosite [7], in the compound $NaBa_2Mn_3F_{11}$ [8], and indirectly via magnetic resonance in $Li_9Fe_3(P_2O_7)_3(PO_4)_2$ [9].

C. Classical spin liquid phase

Having obtained working models of the energy dependence and Q dependence of the excitations, it is natural to investigate whether we can combine these for a complete description. One possibility, inspired by Ref. [47], is a factorization of the dynamical response, which implies that the energy response and Q response are fully decoupled in the system. In such a system, small spin clusters would fluctuate independently of each other. The factorization combines the two theoretical descriptions obtained in Secs. IV B 1 and IV B 2 to read

$$S_{\mathrm{fac}}(Q, \omega, T) = S(Q, T) \times S(\omega, T). \quad (10)$$

The results of this analysis are displayed in Fig. 11, which compares the raw LET data with the model resulting from

Secs. IV B 1 and IV B 2. Here, $S_{\mathrm{fac}}(Q, \omega, T)$ has been normalized, such that the sum of intensities over Q and ω above the elastic line matches that of the experimental data for each temperature.

As expected, the factorization model fails below T_N (Fig. 11, 1.8 and 3 K): It does not capture the spin waves, which is intrinsically a phenomenon with coupled energy response and Q response. In contrast, at the highest shown temperature of 35 K, the factorization model works quite well (apart from the structural feature at very low Q). This is to be expected, since the system is now close to a simple, paramagnetic response with decoupled spin clusters fluctuating independently. At intermediate temperatures of 4 and 8 K, the factorization also does not capture essential features of the data, indicating that the system remains dominated by strongly coupled excitations that are correlated in energy response and Q response. This is in line with the system being in its classical spin liquid regime at these temperatures. This is in agreement with observations in other frustrated compounds, including the pyrochlore $MgCr_2O_4$ [47], which also find that factorization fails in the classical spin liquid regime.

This overall behavior is similar to recent observations in a similar compound, the classical spin liquid h-$YMnO_3$, which is a triangular-lattice Heisenberg magnet with $S = 2$ [48]. These single-crystal neutron studies showed that small 2D clusters fluctuate in the classical spin liquid regime and coexist with the spin waves below the 3D ordering transition in a noninteracting manner. As the temperature is decreased significantly, the spin waves increasingly dominate the picture.

Thus, for Cr-jarosite, the diffuse appearance of the spin waves could also stem from a coexistence and superposition of the 2D dynamics appearing in the classical spin liquid regime above T_N. This could also explain the lack of a complete spin wave gap above the (101) magnetic peak at 1.8 K, if 2D scattering is superimposed on the spin waves. This is supported by the fact that the spin waves in the ordered state, at 1.8 K $\sim T_N/2$, appear strongly damped, as judged from the large Lorentzian broadening obtained by the modeling. Of course, these effects are less clear in powdered samples, and we highlight the need for future single-crystal studies to investigate these phenomena further.

VI. CONCLUSION

We have measured the excitations in well-characterized powder samples of Cr-jarosite. Neutron spectroscopy at low temperatures revealed diffuse spin waves with kagomé zero-mode excitations, which were modeled with linear spin wave
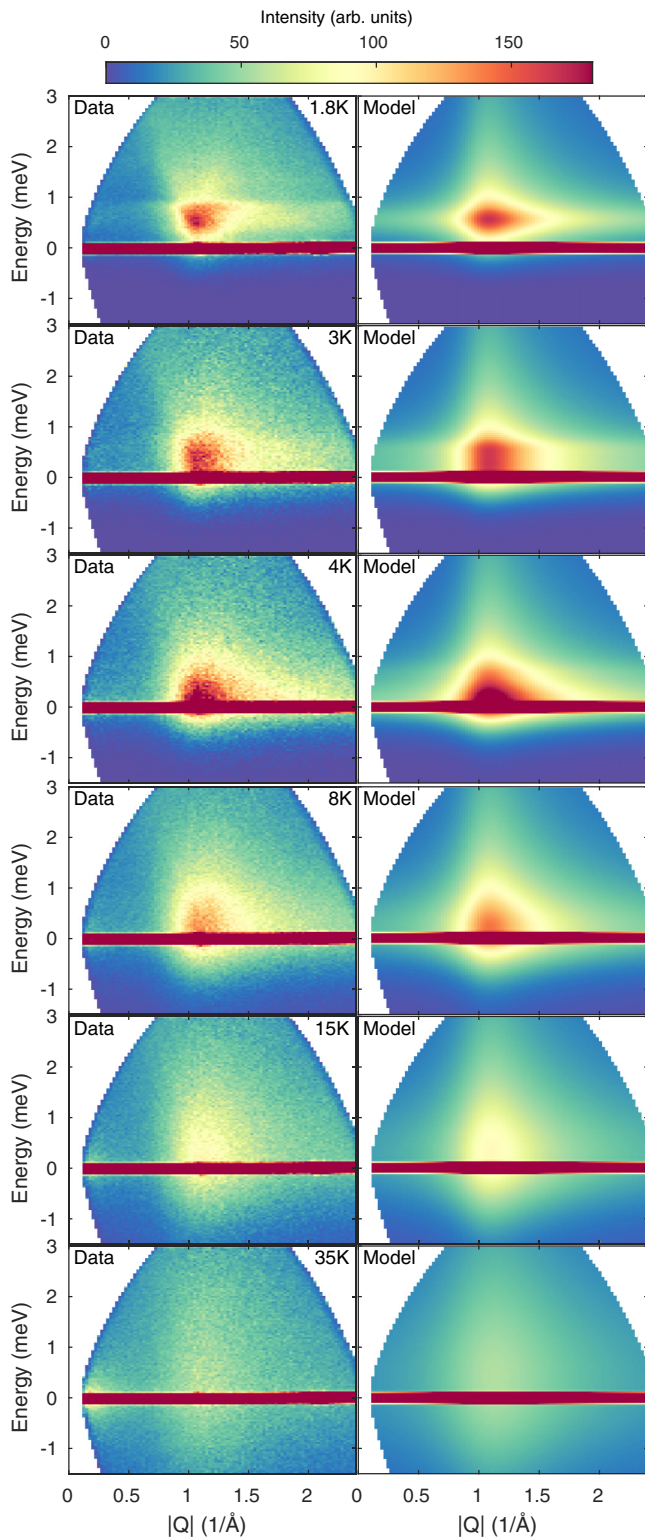
FIG. 11. Left column: raw LET data for selected temperatures. Right column: normalized $S_{\text{fac}}(Q, \omega, T)$ Eq. (10) on a common color scale.

theory to obtain estimates for the exchange couplings. Persistent, diffuse excitations above T_N in the classical spin liquid regime were also observed. The energy response of these was modeled assuming an exponential spin relaxation as well as a

TABLE II. Amount of reactants used in each synthesis, yield of each synthesis, and percentage of the theoretical yield.

Sample No.	K_2SO_4 (g)	Cr (g)	D_2O (ml)	H_2SO_4 (ml)	Yield (g)	Yield (%)
1	4.6596	0.6835	42	2	1.5052	77
2	4.6578	0.6960	42	2	1.4238	72
3	4.6710	0.6775	43	2	1.4403	75
4	4.6657	0.6760	42	2	1.6017	83
5	4.6670	0.6715	42	2	1.72	90
6	4.6818	0.6740	42	2	1.6	84

damped harmonic oscillator model representing the inelastic response below T_N. The Q response was modeled based on 2D cluster excitations. The energy response and Q response were found to be strongly coupled in both the ordered and classical spin liquid regimes, until it decoupled in the fully paramagnetic phase closer to θ_{CW}. This is indicative of classical spin liquid behavior.

APPENDIX A: SYNTHESIS DETAILS

$KCr_3(OD)_6(SO_4)_2$ was synthesized using the redox-hydrothermal method. We dissolved 4.65 g of K_2SO_4 (99.0%; Sigma-Aldrich) in 42 ml D_2O (98%; Cambridge Isotope Laboratories); 2 ml of concentrated sulfuric acid (18 M) were added, and the solution was transferred to an 80-ml Teflon-lined stainless steel hydrothermal reaction vessel, which contained 0.67 g Cr (99.5%; Sigma-Aldrich) pellets. The vessel was placed in a Binder oven and heated at 210 °C for 5 days for samples 1–4, whereas a reaction time of 7 days was used for samples 5 and 6. The product was isolated by filtration, washed with D_2O, and dried in an oven at 60 °C for 4–24 h. The details of the synthesis are summarized in Table II.

APPENDIX B: PXRD

The PXRD diffractograms of all samples were recorded on a Rigaku MiniFlex using a copper target ($K_\alpha = 1.5405$ Å) and collected in the range 5°–90° (2θ) with a step size of 0.02° and a scan rate of 10°/min. Figure 12 shows the PXRD diffractogram of the Cr-jarosite sample. This matches earlier reported diffractograms [19,42].
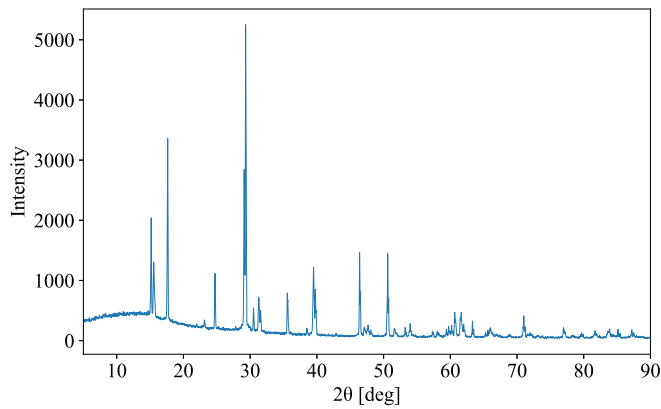
FIG. 12. PXRD spectrum of combined sample, the broad background is from the instrument.

APPENDIX C: SEM

Selected samples including the combined Cr-jarosite were characterized by scanning electron microscopy (SEM) with energy dispersive spectroscopy (EDS) for quantitative analyses of the heavier elements (K, S, and Cr) and sample morphology. SEM-EDS was performed on well-dispersed samples as this allowed us to probe the composition and surface of the individual crystallites, as the primary focus was on sample homogeneity. However, it should be noted that the precision of EDS is improved when measured on the smooth surface of pressed pellets, so the EDS measurement has increased uncertainty.

The measurement was performed on a Hitachi S-4800 scanning electron microscope equipped with an EDS. Approximately 1 mg of sample was dispersed into 1 ml of ethanol by ultrasonification for 15 min. A drop of the suspension was placed on a silicon wafer and then dried at $50\,^{\circ}C$ for 10 min. Subsequently, the surface of the sample was coated with an approximately 15 nm layer of gold. EDS was measured in five random areas of the sample grid using a 15-kV accelerated electron beam and 15 mm working distance. Only sample batches 2 and 3 were measured.

Figure 13 shows the sample at different magnification levels illustrating the particle morphology. The measurements reveal both irregularly shaped and aggregated particles of size 10–50 µm, in agreement with the stacking disorder reported in an earlier study [19]. No additional phases were observed by SEM. The EDS measurements of individual Cr-jarosite crystallites yield a K:Cr:S ratio of 0.99(1):3.3(3):2.00(7) normalized to an S occupancy of 2. This is in rough agreement with the stoichiometric 1:3:2 ratio taking the increased experimental uncertainties into consideration. The Cr content is slightly above the content expected, although with large uncertainties. It may potentially be ascribed to the presence of smaller pieces of unreacted chromium metal in the samples, or reflect large uncertainties of the EDS measurements. We note that several larger chromium metal pieces were present in the isolated product and removed manually before the samples were dried. Therefore we carefully inspected the PXRD, NMR, and neutron data to look for indications of remaining unreacted Cr. The PXRD and neutron data showed no reflections from metallic Cr, and no indication of the antifer-
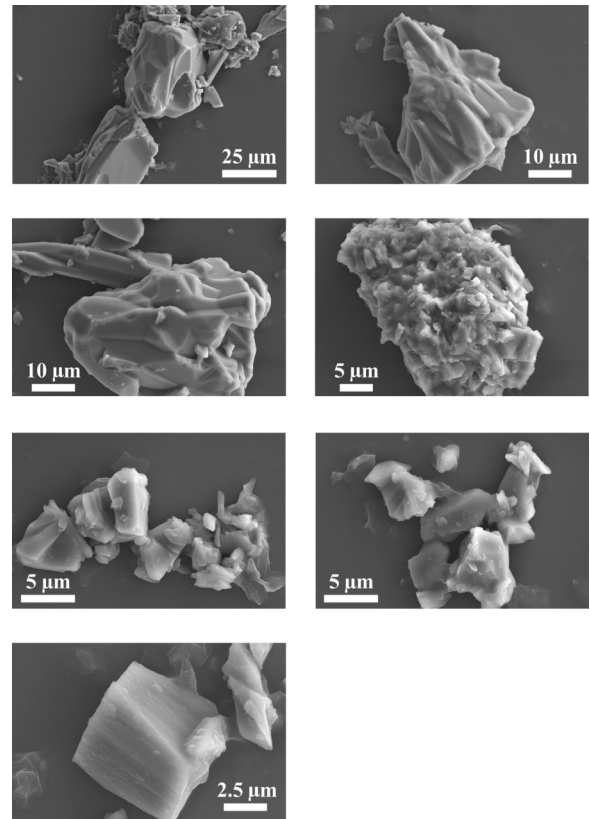

FIG. 13. SEM images of a Cr-jarosite sample at magnifications from 25 to 2.5 µm illustrating the particle morphology.

romagnetic phase transition at 311 K for Cr is observed in the susceptibility data [see Fig. 3(a)]. Thus, if Cr impurities are present, these are negligible.

Based on the experimental uncertainties, the results from ^{2}H MAS NMR provide a more precise quantitative assessment of the Cr and K contents than EDS and PXRD, and we will use the ^{2}H MAS NMR results as the most precise estimate going forward.

APPENDIX D: SIMULATION OF THE ^{2}H MAS NMR SPECTRUM

Figure 14 illustrates the experimental and simulated ^{2}H MAS NMR spectrum of the combined Cr-jarosite sample using the the parameters obtained from fitting of the experimental data in Table III.

APPENDIX E: DERIVATION OF THE Q-DEPENDENT MODEL

We hypothesize that the excitations above T_N originate from two-dimensional dynamics of correlated spin clusters within the kagomé planes. Thus we assume that the 2D excitations will be centered at the 2D ordering vector $(hk) = (10)$, located at $Q_0 = 1.005$ Å^{-1}. Due to the lack of 3D correlations, this scattering will occur as scattering rods around $\mathbf{Q} = (10l)$. To obtain the observed pattern, the rods must then be powder-averaged in three-dimensional (hkl) space. This is sketched geometrically in Fig. 15. Here the shaded area represents the overlap between the sphere of (hkl) points of constant length, Q, and the cylindrical rod at $(10l)$, which has

TABLE III. ^{2}H MAS NMR parameters for the combined sample recorded at 33 kHz spinning speed. The CSA parameters (Δ and η_σ), quadrupole coupling (C_Q and η_Q), signal intensities, and Cr site and K site vacancies were found by fitting of the recorded ^{2}H MAS NMR spectrum [34]. The CSA parameters are given in the Haeberlen convention [35], where β is an Euler angle between the principal axis of the CSA and quadrupole tensor [36]. The vacancies are given per mole. The errors were estimated from the upper and lower boundaries of the fitted parameters.

Site	δ_{iso} (ppm)	Δ (ppm)	η_σ	C_Q (MHz)	η_Q	β (deg)	Intensity (%)
Cr$_2$-OD (D)	872(10)	$-1020(100)$	1.00(10)	0.216(40)	0.10(10)	45(10)	15(1)
Cr$_2$-OD (K)	828(5)	$-935(50)$	1.00(10)	0.214(10)	0.09(10)	55(5)	69(1)
Cr$_2$-OD	229(5)	830(50)	0.00(10)	0.101(5)	0.64(10)	74(10)	10(1)
D$_n$O (sharp)	11(1)	0(10)	0.00(10)	0.100(5)	0.00(10)	0(5)	<1
D$_n$O	7(2)	0(10)	0.00(10)	0.050(5)	0.00(10)	0(5)	6(1)
x:	0.085(5)	Cr (%):	2.8(3)	n:	0.41(10)	K (%):	~14–20

its smallest Q value at (100), with the length $Q = Q_0$. The shape of the scattering intensity is thus related to the overlap volume, which must be calculated.

The (hk) rod has width dw, and the Q sphere has width $dq \ll Q$ as illustrated in Fig. 15. Assuming that the intersection is not curved appreciably over the area, then the overlap area is $A = h\,dw$, where h is the effective height. h is also the hypotenuse in the triangle as indicated, and can be written as $h = dq/\sin\phi$, which thus makes the area $A = dw\,dq/\sin\phi$. By realizing that the ϕ is equivalent in the triangles sketched in the left and right panels in Fig. 15, then it can be related to the scattering vectors via $\cos\phi = Q_0/Q$.

The scattering intensity can be found as the ratio between the overlap volume, $V_o = A\,dw$, and the volume of the spherical shell, $V_s = 4\pi Q^2 dQ$:

$$\mathcal{V}(Q) = \frac{V_o}{V_s} = \frac{dq\,dw^2/\sin\phi}{4\pi dqQ^2} \propto \frac{1}{Q\sqrt{Q^2 - Q_0^2}}, \qquad \text{(E1)}$$

where the constants can be accounted for in an overall scaling factor. Now, this expression is only valid for $Q > Q_0$ and takes a value of zero for $Q < Q_0$. The expression diverges at $Q = Q_0$ in a square-root manner, making the integral $\int \mathcal{V}(Q)dQ$ take a finite value. This expression was also found in Ref. [45],
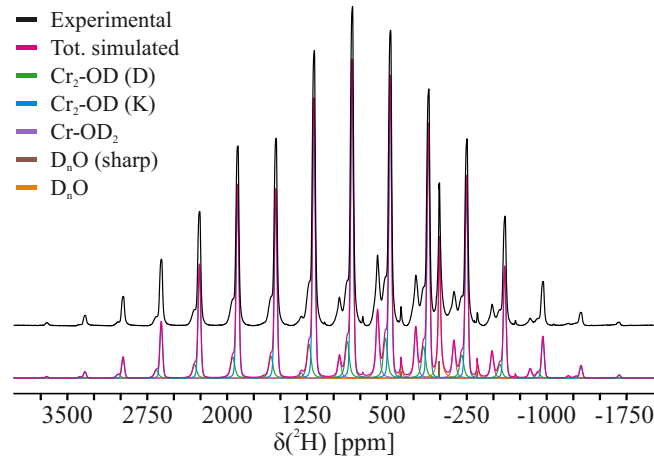
which also finds a modification to Eq. (E1) close to the divergence that is unnecessary for our purpose. These results are, in turn, a correction of the classical results for 2D line shapes by Warren [46].

A way to account for the short-range correlations in the magnetic system is to assume a finite-size broadening of the value of Q_0. We obtain this by a convolution of $\mathcal{V}(Q)$ with a Lorentzian to model smearing by short-ranged correlations with correlation length $\xi = 1/\gamma$, where γ is the full width at half maximum of the Lorentzian. Thus the resulting convoluted line shape is

$$C_L(Q) = |f(Q)|^2 \qquad \text{(E2)}$$
$$\times \int_0^\infty \frac{1}{Q'\sqrt{Q'^2 - Q_0^2}} \frac{\gamma^2}{(\gamma/2)^2 + (Q' - Q)^2}\,dQ'.$$

Here, the magnetic form factor $f(Q)$ for Cr^{3+} has been added using tabulated values from Ref. [49]. The intensity has zero value for small values of Q but starts to increase when the Lorentzian just touches Q_0. As Q approaches Q_0 the value increases rapidly. At values clearly larger than Q_0, the value slowly decays. Thus the asymmetric peak shape is caused by the asymmetry of the overlap function $\mathcal{V}(Q)$. As an additional result of the convolution, the peak position is displaced to a value of Q slightly larger than Q_0.

FIG. 14. Experimental and simulated ^{2}H MAS NMR spectrum (Hahn echo) of combined sample recorded with 33 kHz spinning speed using the parameters in Table III.
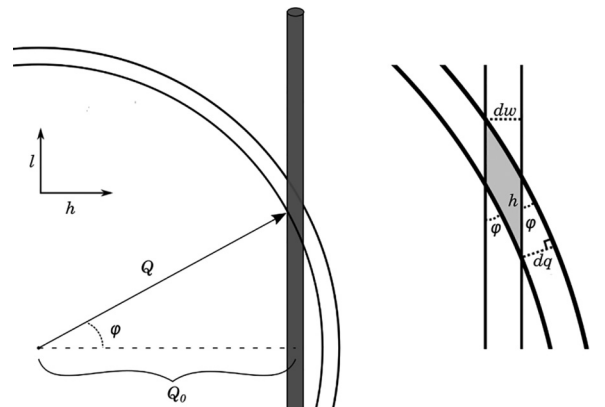

FIG. 15. Reciprocal lattice representation of scattering by 2D reflections.

[1] L. Balents, Spin liquids in frustrated magnets, Nature (London) **464**, 199 (2010).

[2] J. Wen, S. L. Yu, S. Li, W. Yu, and J. X. Li, Experimental identification of quantum spin liquids, npj Quantum Mater. **4**, 12 (2019).

[3] L. Savary and L. Balents, Quantum spin liquids: A review, Rep. Prog. Phys. **80**, 016502 (2017).

[4] J. Knolle and R. Moessner, A field guide to spin liquids, Annu. Rev. Condens. Matter Phys. **10**, 451 (2019).

[5] J. R. Chamorro, T. M. McQueen, and T. T. Tran, Chemistry of quantum spin liquids, Chem. Rev. **121**, 2898 (2021).

[6] P. Mendels and A. S. Wills, Kagomé antiferromagnets: Materials vs. spin liquid behaviors, in *Introduction to Frustrated Magnetism: Materials, Experiments, Theory*, edited by C. Lacroix, P. Mendels, and F. Mila, Springer Series in Solid-State Sciences (Springer, New York, 2011), Vol. 164, pp. 207–236.

[7] K. Matan, D. Grohol, D. G. Nocera, T. Yildirim, A. B. Harris, S. H. Lee, S. E. Nagler, and Y. S. Lee, Spin Waves in the Frustrated Kagomé Lattice Antiferromagnet $KFe_3(OH)_6(SO_4)_2$, Phys. Rev. Lett. **96**, 247201 (2006).

[8] S. Hayashida, H. Ishikawa, Y. Okamoto, T. Okubo, Z. Hiroi, G. J. Nilsen, H. Mutka, and T. Masuda, Zero-energy excitation in the classical kagome antiferromagnet $NaBa_2Mn_3F_{11}$, Phys. Rev. B **101**, 214409 (2020).

[9] E. Kermarrec, R. Kumar, G. Bernard, R. Hénaff, P. Mendels, F. Bert, P. L. Paulose, B. K. Hazra, and B. Koteswararao, Classical Spin Liquid State in the $S = \frac{5}{2}$ Heisenberg Kagome Antiferromagnet $Li_9Fe_3(P_2O_7)_3(PO_4)_2$, Phys. Rev. Lett. **127**, 157202 (2021).

[10] D. Grohol, D. G. Nocera, and D. Papoutsakis, Magnetism of pure iron jarosites, Phys. Rev. B **67**, 064401 (2003).

[11] D. G. Nocera, B. M. Bartlett, D. Grohol, D. Papoutsakis, and M. P. Shores, Spin frustration in 2D kagome lattices: A problem for inorganic synthetic chemistry, Chem. Eur. J. **10**, 3850 (2004).

[12] D. Grohol, K. Matan, J. H. Cho, S. H. Lee, J. W. Lynn, D. G. Nocera, and Y. S. Lee, Spin chirality on a two-dimensional frustrated lattice, Nat. Mater. **4**, 323 (2005).

[13] K. Matan, B. M. Bartlett, J. S. Helton, V. Sikolenko, S. Mat'aš, K. Prokeš, Y. Chen, J. W. Lynn, D. Grohol, T. J. Sato, M. Tokunaga, D. G. Nocera, and Y. S. Lee, Dzyaloshinskii-Moriya interaction and spin reorientation transition in the frustrated kagome lattice antiferromagnet, Phys. Rev. B **83**, 214406 (2011).

[14] T. Fujita, H. Yamaguchi, S. Kimura, T. Kashiwagi, M. Hagiwara, K. Matan, D. Grohol, D. G. Nocera, and Y. S. Lee, High-field multifrequency ESR in the $S = \frac{5}{2}$ kagome-lattice antiferromagnet $KFe_3(OH)_6(SO_4)_2$, Phys. Rev. B **85**, 094409 (2012).

[15] R. A. Klein, J. P. Walsh, S. M. Clarke, Y. Guo, W. Bi, G. Fabbris, Y. Meng, D. Haskel, E. E. Alp, R. P. Van Duyne, S. D. Jacobsen, and D. E. Freedman, Impact of pressure on magnetic order in jarosite, J. Am. Chem. Soc. **140**, 12001 (2018).

[16] A. Mook, R. R. Neumann, J. Henk, and I. Mertig, Spin Seebeck and spin Nernst effects of magnons in noncollinear antiferromagnetic insulators, Phys. Rev. B **100**, 100401(R) (2019).

[17] D. Grohol and D. G. Nocera, Hydrothermal oxidation-reduction methods for the preparation of pure and single crystalline alunites: Synthesis and characterization of a new series of vanadium jarosites, J. Am. Chem. Soc. **124**, 2640 (2002).

[18] D. Papoutsakis, D. Grohol, and D. G. Nocera, Magnetic properties of a homologous series of vanadium jarosite compounds, J. Am. Chem. Soc. **124**, 2647 (2002).

[19] S. Janas, M. B. Sørensen, A. B. Andersen, M. Juelsholt, M. Boehm, K. S. Pedersen, K. M. Jensen, K. Lefmann, and U. G. Nielsen, Structural characterization and magnetic properties of chromium jarosite $KCr_3(OD)_6(SO_4)_2$, Phys. Chem. Chem. Phys. **22**, 25001 (2020).

[20] K. Okuta, S. Hara, H. Sato, Y. Narumi, and K. Kindo, Observation of 1/3 magnetization-plateau-like anomaly in $S = 3/2$ perfect kagomé lattice antiferromagnet $KCr_3(OH)_6(SO_4)_2$(Cr-jarosite), J. Phys. Soc. Jpn. **80**, 063703 (2011).

[21] S. Okubo, R. Nakata, S. Ikeda, N. Takahashi, T. Sakurai, W. Zhang, H. Ohta, T. Shimokawa, T. Sakai, K. Okuta, S. Hara, and H. Sato, Dzyaloshinsky-Moriya interaction and the ground state in $S = 3/2$ perfect kagome lattice antiferromagnet $KCr_3(OH)_6(SO_4)_2$(Cr-jarosite) studied by X-band and high-frequency ESR, J. Phys. Soc. Jpn. **86**, 024703 (2017).

[22] U. G. Nielsen, J. Majzlan, and C. P. Grey, Determination and quantification of the local environments in stoichiometric and defect jarosite by solid-state ^2H NMR spectroscopy, Chem. Mater. **20**, 2234 (2008).

[23] U. G. Nielsen, I. Heinmaa, A. Samoson, J. Majzlan, and C. P. Grey, Insight into the local magnetic environments and deuteron mobility in jarosite ($AFe_3(SO_4)_2(OD,OD_2)_6$, A = K, Na, D_3O) and hydronium alunite (($D_3O)A_{l3}(SO_4)_2(OD)_6$), from variable-temperature ^2H MAS NMR spectroscopy, Chem. Mater. **23**, 3176 (2011).

[24] A. S. Wills, G. S. Oakley, D. Visser, J. Frunzke, A. Harrison, and K. H. Andersen, Short-range order in the topological spin glass $(D_3O)Fe_3(SO_4)_2(OD)_6$ using xyz polarized neutron diffraction, Phys. Rev. B **64**, 094436 (2001).

[25] D. Grohol and D. G. Nocera, Magnetic disorder in the frustrated antiferromagnet jarosite arising from the $H_3O^+ \cdots OH^-$ interaction, Chem. Mater. **19**, 3061 (2007).

[26] W. G. Bisson and A. S. Wills, Anisotropy-driven spin glass transition in the kagome antiferromagnet hydronium jarosite, $(H_3O)Fe_3(SO_4)_2(OH)_6$, J. Phys.: Condens. Matter **20**, 452204 (2008).

[27] A. S. Wills and W. G. Bisson, Elemental analysis and magnetism of hydronium jarosites—model kagome antiferromagnets and topological spin glasses, J. Phys.: Condens. Matter **23**, 164206 (2011).

[28] H. J. Spratt, M. Avdeev, M. C. Pfrunder, J. McMurtrie, L. Rintoul, and W. N. Martens, Location of hydrogen atoms in hydronium jarosite, Phys. Chem. Miner. **41**, 505 (2014).

[29] M. G. Townsend, G. Longworth, and E. Roudaut, Triangular-spin, kagome plane in jarosites, Phys. Rev. B **33**, 4919 (1986).

[30] A. Keren, K. Kojima, L. P. Le, G. M. Luke, W. D. Wu, Y. J. Uemura, M. Takano, H. Dabkowska, and M. J. P. Gingras, Muon-spin-rotation measurements in the *kagomé* lattice systems: Cr-jarosite and Fe-jarosite, Phys. Rev. B **53**, 6451 (1996).

[31] A. S. Wills, A study of experimental kagomé antiferromagnets based on the jarosite, Ph.D. thesis, The University of Edinburgh, 1996.

[32] A. S. Wills, Conventional and unconventional orderings in the jarosites, Can. J. Phys. **79**, 1501 (2001).

[33] S. H. Lee, C. Broholm, M. F. Collins, L. Heller, A. P. Ramirez, C. Kloc, E. Bucher, R. W. Erwin, and N. Lacevic, Less than

50% sublattice polarization in an insulating $S = 3/2$ *kagomé* antiferromagnet at $T \approx 0$, Phys. Rev. B **56**, 8091 (1997).

[34] S. W. Franssen and A. Kentgens, ssNake: A cross-platform open-source NMR data processing and fitting application, J. Magn. Reson. **301**, 56 (2019).

[35] R. Harris, E. Becker, S. De Menezes, P. Granger, R. Hoffman, and K. Zilm, Further conventions for NMR shielding and chemical shifts (IUPAC Recommendations 2008), Magn. Reson. Chem. **46**, 582 (2008).

[36] J. Skibsted, N. C. Nielsen, H. Bildsøe, and H. J. Jakobsen, ^{51}V MAS NMR spectroscopy: determination of quadrupole and anisotropic shielding tensors, including the relative orientation of their principal-axis systems, Chem. Phys. Lett. **188**, 405 (1992).

[37] A. D. Taylor, M. Arai, S. M. Bennington, Z. A. Bowden, R. Osborn, K. Andersen, W. G. Stirling, T. Nakane, K. Yamada, and D. Welz, First results from the UK-Japanese spectrometer MARI, in *International Collaboration on Advanced Neutron Sources (ICANS XI)* (U.S. Department of Energy, Washington, DC, 1990), pp. 705–710.

[38] R. I. Bewley, J. W. Taylor, and S. M. Bennington, LET, a cold neutron multi-disk chopper spectrometer at ISIS, Nucl. Instrum. Methods Phys. Res. A **637**, 128 (2011).

[39] O. Arnold, J. C. Bilheux, J. M. Borreguero, A. Buts, S. I. Campbell, L. Chapon, M. Doucet, N. Draper, R. Ferraz Leal, M. A. Gigg, V. E. Lynch, A. Markvardsen, D. J. Mikkelson, R. L. Mikkelson, R. Miller, K. Palmen, P. Parker, G. Passos, T. G. Perring, P. F. Peterson *et al.*, Mantid - Data analysis and visualization package for neutron scattering and μSR experiments, Nucl. Instrum. Methods Phys. Res. A **764**, 156 (2014).

[40] R. A. Ewings, A. Buts, M. D. Le, J. van Duijn, I. Bustinduy, and T. G. Perring, HORACE: Software for the analysis of data from single crystal spectroscopy experiments at time-of-flight neutron instruments, Nucl. Instrum. Methods Phys. Res. A **834**, 132 (2016).

[41] S. Toth and B. Lake, Linear spin wave theory for single-Q incommensurate magnetic structures, J. Phys.: Condens. Matter **27**, 166002 (2015).

[42] E. Grube, A. S. Lipton, and U. G. Nielsen, Identification of hydrogen species in alunite-type minerals by multi-nuclear solid-state NMR spectroscopy, Phys. Chem. Miner. **46**, 299 (2018).

[43] T. Yildirim and A. B. Harris, Magnetic structure and spin waves in the Kagomé jarosite compound $KFe_3(SO_4)_2(OH)_6$, Phys. Rev. B **73**, 214446 (2006).

[44] B. Fåk and B. Dorner, Phonon line shapes and excitation energies, Phys. B (Amsterdam) **234-236**, 1107 (1997).

[45] D. Yang and R. F. Frindt, Powder x-ray diffraction of two-dimensional materials, J. Appl. Phys. **79**, 2376 (1996).

[46] B. E. Warren, X-ray difraction in random layer lattices, Phys. Rev. **59**, 693 (1941).

[47] X. Bai, J. A. M. Paddison, E. Kapit, S. M. Koohpayeh, J. J. Wen, S. E. Dutton, A. T. Savici, A. I. Kolesnikov, G. E. Granroth, C. L. Broholm, J. T. Chalker, and M. Mourigal, Magnetic Excitations of the Classical Spin Liquid $MgCr_2O_4$, Phys. Rev. Lett. **122**, 097201 (2019).

[48] S. Janas, J. Lass, A. E. Tutueanu, M. L. Haubro, C. Niedermayer, U. Stuhr, G. Xu, D. Prabhakaran, P. P. Deen, S. Holm-Dahlin, and K. Lefmann, Classical Spin Liquid or Extended Critical Range in h-$YMnO_3$? Phys. Rev. Lett. **126**, 107203 (2021).

[49] P. J. Brown, Form factors for 3d transition elements and their ions, 2020, https://www.ill.eu/sites/ccsl/ffacts/ffactnode5.html.